Topological spin textures and topological Hall effect in centrosymmetric magnetic nanoparticles

Ahsan Ullah,* Balamurugan Balasubramanian, Bibek Tiwari, Bharat Giri, David J. Sellmyer,† Ralph Skomski,† and Xiaoshan Xu

Department of Physics and Astronomy and Nebraska Center for Materials and Nanoscience, University of Nebraska, Lincoln, Nebraska 68588, USA

(Received 15 May 2023; revised 28 September 2023; accepted 14 November 2023; published 29 November 2023)

Although topological spin textures are not commonly found in centrosymmetric magnetic systems, noncoplanar monodomain magnetic states such as flower and curling states do emerge due to the contribution of surfaces and edges in nanoparticles. In this work, we studied the topological nature of these intriguing noncoplanar spin textures and their manifestation in electric transport phenomena due to the *Berry phase* accumulation. Specifically, we calculated the topological charges Q associated with these spin textures and the corresponding topological Hall effect. We assessed these spin textures across various particle sizes and along magnetic hysteresis loops and mapped the spin structures in confined geometries using magnetic force microscopy. We show that Q, as a fractional number, increases with particle size and saturates as the system transits from the flower state to the curling state. Along magnetic hysteresis loops, smaller particles that show flower states in zero field, exhibit a peak in Q near the coercive field, a signature of the topological Hall effect demonstrated in other systems. In contrast, larger particles that show curling states during the magnetization reversal, exhibit transitions between the homogeneous state, flower state, and curling state, which generates jumps in Q and the topological Hall effects. These results reveal the rich topological nature of centrosymmetric magnetic nanoparticles, offer control using magnetic field and probe using electric transport, suggesting promising potential applications.

DOI: 10.1103/PhysRevB.108.184432

I. INTRODUCTION

The behavior of topological spin textures in continuous parameter space has fascinated researchers due to their intriguing properties and potential applications [1–3]. These distinctive spin configurations are most notably observed as skyrmions [4–6] in noncentrosymmetric bulk materials [7–9], thin films [10], multilayer films [2,11,12], and even as meron [13–15], among others. Nanostructured thin films, including nanogranular (polycrystalline) materials and ensembles of nanoparticles, also exhibit magnetic and transport properties very different from homogeneous thin films, representing the presence of topological spin textures [16–19].

The presence of topological spin textures in magnetic nanoparticles recently attracted significant attention due to their unique size-dependent properties and potential applications in data storage, biomedicine, and spintronics [20,21]. It has been reported that isolated nanoparticles of B-20 crystal structures can exhibit geometrically stabilized skyrmionic spin textures [22,23], due to the Dzyashinski-Moriya interaction (DMI) which is enabled by the broken inversion symmetry and favors perpendicular neighboring spin alignments [24–26].

On the other hand, topological spin textures are not expected in noninteracting centrosymmetric magnetic nanoparticles due to the lack of DMI. That said, noncoplanar single-domain states such as flower and curling states have been identified in these systems [20,27–37]. These complex spin textures result from the competition between the exchange interaction, anisotropy, and demagnetization which are sensitive to the shape and size of the nanoparticles. Despite the intriguing physics and significant technological potentials, the topological nature of these spin textures, and their manifestation in electronic transport, has not been systematically studied.

Topological spin textures can manifest in electric transport because the exchange interaction between the local and itinerant spins causes rapid rotations of the latter and modifies the electronic trajectory [38]. Quantum mechanically, under the adiabatic conditions [39,40], itinerant electrons remain in the local eigenstates defined by the local spins. For noncoplanar spin texture, the wave function of itinerant electrons accumulates a phase factor γ, known as the *Berry* phase [41], which can be found through integration over Berry curvature $\vec{B}_c$ [42] that the itinerant electrons sense. Berry curvature $\vec{B}_c$ is proportional to solid angle Ω created by noncoplanar spins as showin in Fig. 1(a) and in continuum space is determined by the spin textures as

$$\vec{B}_c = -\epsilon_{ijk}\frac{1}{2}\boldsymbol{S}\cdot(\partial_i\boldsymbol{S}\times\partial_j\boldsymbol{S}), \tag{1}$$

where $\boldsymbol{S}(\boldsymbol{r})$ is the unit vector describing the spin direction at position $\boldsymbol{r}$, and ϵ_{ijk} is the antisymmetric tensor. The surface integral $\gamma = \int \vec{B}_c \cdot d\vec{A}$, or the Berry phase accumulated by an itinerant electron going around the spin texture, is nonzero for topological spin textures. Correspondingly, one can

*aullah@huskers.unl.edu
†Deceased.

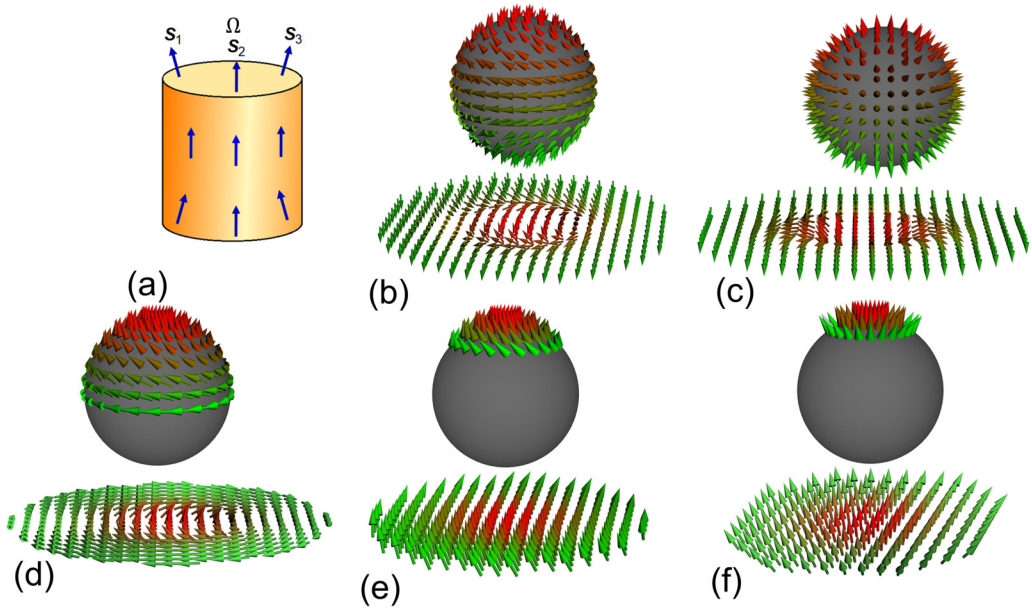

FIG. 1. (a) Three noncoplanar spins $\boldsymbol{S}_1$, $\boldsymbol{S}_2$, and $\boldsymbol{S}_3$ creates a solid angle $\Omega = \boldsymbol{S}_1$. $(\boldsymbol{S}_2 \times \boldsymbol{S}_3)$ leads to nonzero Berry phase and topological charge Q. Topological spin textures in a two-dimensional space which can be mapped onto a spherical surface: (b) and (c) are Bloch and Néel skyrmions, respectively, where the topological charge is $Q = 1$ [6,12,13]. (d) Spin vortex where $Q = {}^1/_2$ [6,13,15]. (e) and (f) are curling and flower states, respectively, where $Q < {}^1/_2$.

define topological charge $Q = \frac{1}{2\pi} \int \vec{B}_c \cdot d\vec{A}$. Q equals ± 1 for skyrmions, hence it is also known as the skyrmion number. Q is fractional for the flower and the curling states (see Fig. 1).

The way the itinerant spin follows the local spin can be described using an *emergent magnetic field* $\vec{B}_e = \frac{\hbar}{e}\vec{B}_c$ [4] which deflects the electrons and leads to an additional Hall effect known as the topological Hall effect (THE) [7,43]. The resistivity due to THE can be expressed as

$$\rho_{\mathrm{THE}} = PR_0 \langle B_e \rangle = PR_0 \frac{hQ}{eA}, \tag{2}$$

where P is the spin polarization, R_0 is the Hall coefficient, and A is the area of the spin texture. This signature in electrical transport provides a means to probe the topological spin texture, in addition to direct observation using magnetic imaging. The latter can be challenging for nanoparticles due to the need for high resolution. Hence investigating topological charges and THE due to noncoplanar states in nanoparticles with finite Q is an interesting avenue for exploration, considering their application potential in spintronics at high temperatures.

In this work, through micromagnetic modeling and simulations, and magnetic force microscopy (MFM), we studied the noninteracting centrosymmetric nanoparticles in terms of their spin texture and topological charge Q, which is proportional to the Berry curvature and emergent magnetic field that leads to THE. The focus is on the particle size near the coherence radius R_{coh} (in the range of 10–30 nm) where the transition from flower state to curling state occurs [27–29,34]. We show that in zero field, the topological charge increases with particle size when the radius is less than R_{coh} and saturates in the curling state. Along the magnetic hysteresis loop, a maximum Q occurs near the coercive field, as observed in other systems [7–10,16–19]. More intriguingly, for particles that are stable in the curling states in zero fields, magnetic hysteresis contains the transitions between homogeneous, flower, and curling states, causing jumps in the topological Hall signal.

II. METHODS

Throughout the paper, we express the local magnetization as $\boldsymbol{M}(\boldsymbol{r}) = M_s \boldsymbol{S}(\boldsymbol{r})$, where $\mathbf{S}(\mathbf{r})$ is a unit vector. We employ an analytical approach, utilizing an approximate Hamiltonian to describe the flower state. For the curling mode, we used exact solutions expressed in terms of Bessel functions. The local configuration $\boldsymbol{M}(\boldsymbol{r}) = M_s \boldsymbol{S}(\boldsymbol{r})$ is determined using the energy function given by [34,44]

$$\mathcal{E} = \int \left\{ A_e \left[\nabla \left(\frac{\boldsymbol{M}}{M_s} \right) \right]^2 - K_1 \frac{(\boldsymbol{n} \cdot \boldsymbol{M})^2}{M_s^2} - \mu_0 \boldsymbol{M} \cdot \boldsymbol{H} - \frac{\mu_0}{2} \boldsymbol{M} \cdot \boldsymbol{H}_d(\boldsymbol{M}) \right\} \mathrm{d}V. \tag{3}$$

The exchange stiffness A_e parametrizes the interatomic exchange energy $\eta_A = A_e (\nabla \boldsymbol{S})^2$, and K_1 is the uniaxial anisotropy assumed to be along the c axis in the z direction, which includes both magnetocrystalline (K_1) and shape-anisotropy contributions. There are three magnetostatic terms in Eq. (3), namely, the Zeeman interactions with the external magnetic field H, and the magnetostatic self-interaction energy described by the demagnetizing field $\boldsymbol{H}_d(\boldsymbol{M})$. Physically $\boldsymbol{M}(\boldsymbol{r})$ corresponds to local and global minima of the integrated energy in Eq. (3). To explore the topological spin textures and THE numerically, the topological charge (Q) was extracted from the spin structure.

Micromagnetic simulations were performed using UBERMAG supported by OOMMF [45,46]. Different nanoparticle

TABLE I. The micromagnetic parameters, carrier density, spin polarization, and ordinary Hall coefficient used to calculate the topological charge and topological Hall effect [34,36,47].

Substance	A_e (pJ/m)	$\mu_0 M_s$ (T)	K_1 (MJ/m^3)	T_c (K)	R_{coh} (nm)	P	n (1/cm^3)	$R_0 = 1/ne$ (m^3/C)
Toy model	11	2.3	0.2		12			
Co	10.3	1.76	0.53	1388	10	0.45	9×10^{22}	5×10^{22}
Fe	21	2.15	0.048	1043	11.7	0.4	8.45×10^{22}	7.38×10^{-11}
Ni	7.69	0.61	−0.0048	631	24.7	0.4	9.1×10^{22}	-6.8×10^{22}

sizes were considered in our simulations to study the flower state and curling mode, and the effect of the magnetic field on these spin textures. The computational cell size was set to be less than 1.9 nm, significantly smaller than the exchange length l_{ex} [34]. For reference, the values of the micromagnetic parameters and other constants are provided in Table I. For evaluating the THE in the nanoparticles, we employed Eq. (2), which allowed us to determine THE as a function of $Q(H)$ and the nanoparticle's area. To probe topological spin textures using MFM the Co ferromagnetic dots were fabricated through electron-beam lithography and evaporation in an ultrahigh vacuum using an electron-beam gun. The circular nanodot patterns were defined on thermally oxidized Si substrates with positive photoresists.

The bilayer-positive photoresists PMMA950/MMA EL6 were exposed to an electron beam and the lift-off method was used to create the circular pattern. The fabricated circular arrays were arranged in a trilayer structure of Ti/Co/SiO_2, with respective thicknesses of $\sim$ 20 nm for Ti, $\sim$ 40 nm for Co, and $\sim$ 20 nm for the SiO_2 layer to prevent oxidation. The layer thicknesses were monitored during growth using a quartz balance. The circular layered structure was grown by e-beam evaporation in a UHV system. The base pressure was in the range of 1×10^{-8} torr. The evaporation pressure was less than 5×10^{-7} torr. By a lift-off process, the photoresist was removed and dots with designed sizes remained on top of the Si surface.

To examine the topography and magnetic images of the samples, we used a Bruker Dimension Icon atomic force microscope (AFM) at room temperature, performing MFM in constant height mode (single pass). In the MFM experiment, we employed the AC mode of the instrument to detect the magnetic forces between the cantilever tip and the surface of circular dots under ambient conditions. To mitigate the impact of stray fields, we utilized a low-moment CoCr tip. The tip-to-surface distance was maintained within the range of 20–30 nm.

III. CALCULATIONS AND RESULTS

The topological spin textures can develop in nanoparticles of various shapes, as depicted in Fig. 2. All structures in Fig. 2 exhibit axial symmetry, that is, the magnetic easy axis is the c axis along the z direction, and C_3, C_4, or C_∞ rotations reproduce the original spin structure, respectively. Equation (1) means that the Berry curvature and topological charge are unique functions of the spin structure $\mathbf{S}(\mathbf{r})$, which is determined by the magnetic interactions and sample geometry. We represent the $\mathbf{S}(\mathbf{r})$ with the following expression [28]:

$$\boldsymbol{S}(\boldsymbol{r}) = \sin\Theta(r)\cos\Phi(r)\boldsymbol{e}_x + \sin\Theta(r)\cos\Phi(r)\boldsymbol{e}_y + \cos\Theta(r)\boldsymbol{e}_z. \tag{4}$$

Here, $\boldsymbol{e}_x$, $\boldsymbol{e}_y$, and $\boldsymbol{e}_z$ are unit vectors along the x, y, and z directions, respectively, and $r = (x^2 + y^2)^{1/2}$. The angles $\Theta(\boldsymbol{r})$ and $\Phi(\boldsymbol{r})$ represent the polar and azimuthal angles, respectively. The flower state and the curling state both exhibit slight deviations from the homogeneous magnetization along the easy axis (z axis). The xy component of $\mathbf{S}$ can be written as

$$\boldsymbol{S}_{xy}(\boldsymbol{r}) = \sin\Theta(r)\cos\Phi(r)\boldsymbol{e}_x + \sin\Theta(r)\cos\Phi(r)\boldsymbol{e}_y, \tag{5}$$

Which corresponds to the radial direction for the flower state and the azimuthal direction for the curling state. Utilizing cylindrical coordinates [$\mathbf{r} = (\rho, \varphi, z)$], we can express the flower state and the curling state using $\Phi(\boldsymbol{r}) = \varphi$

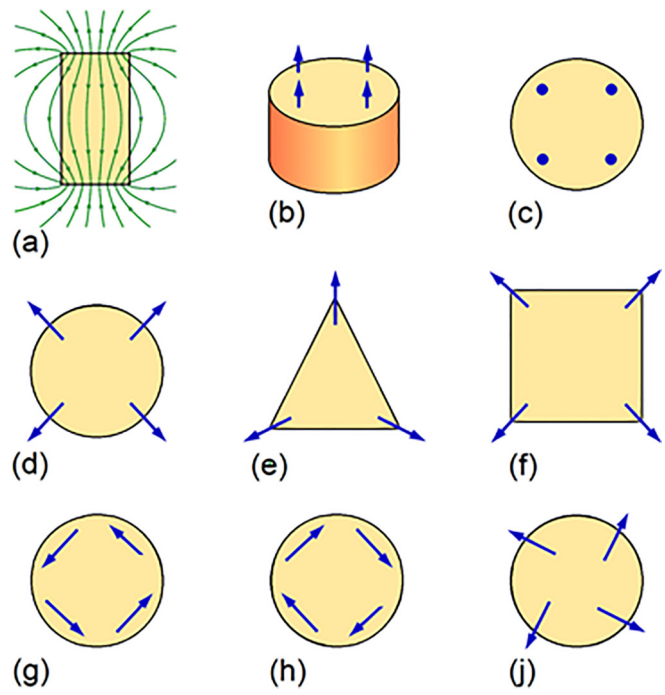

FIG. 2. Examples of spin structures in small nanoparticles: (a) stray field distribution in the middle and at the edges of a cylindrical nanoparticle; (b),(c) uniform magnetization; (d) flower state in a cylindrical particle; (e),(f) flower states in prismatic nanoparticles; (g),(h) vortex states of opposite chirality; and (j) mixed state. The spins $\mathbf{S}(\boldsymbol{r})$ are shown as blue arrows.

and $\Phi(\boldsymbol{r}) = \varphi \pm \pi/2$, respectively. To better visualize these states, we present the vector three-dimensional plot for the flower state without any helicity ($\Lambda = 0$) $\Phi(\mathbf{r}) = \varphi$ and for the curling state with finite helicity ($\Lambda = \pm\pi/2$) $\Phi(\mathbf{r}) = \varphi \pm \pi/2$ in Figs. 1(e) and 1(f) and Supplemental Material Fig. S1. In cylindrical coordinates, we can write $\boldsymbol{S} = S_{xy}(\boldsymbol{r})\boldsymbol{e}_R + S_z\boldsymbol{e}_z = \sin\Theta(r)\boldsymbol{e}_\rho + S_z\boldsymbol{e}_z$, where $\boldsymbol{e}_R = \cos\Phi(\boldsymbol{r})\boldsymbol{e}_x + \sin\Phi(\boldsymbol{r})\boldsymbol{e}_y$ and $S_{xy}(\boldsymbol{r}) = \sin\Theta(r)$. The energy functional for magnetic nanoparticles, considering a small deviation from the easy axis, can be expressed as (for further details, refer to the Supplemental Material [48])

$$\mathcal{E} = \int [A_e[\nabla \boldsymbol{S}_{xy}(\boldsymbol{r})]^2 + K[\boldsymbol{S}_{xy}(\boldsymbol{r})]^2 + \tfrac{1}{2}\mu_0(H - H_d)M_s\boldsymbol{S}_{xy}(\boldsymbol{r})^2 - \tfrac{1}{2}\mu_0 M_s H_F \sin\Theta]\mathrm{d}V. \quad (6)$$

In Eq. (6), the demagnetization field $\boldsymbol{H}_d(\boldsymbol{M}) = -D\boldsymbol{M}_z$ along the z axis results in a flux closure state resembling a curling. On the other hand, the demagnetization field H_F at the edges or corners leads to a slight tilt of the spin representing nonuniform magnetization inside the nanoparticles. Notably, in nanoparticles with a flower state, the curling state does not exist ($H_d \approx 0$), and in the presence of a curling state, there will not be any flower state ($H_F = 0$) [29].

The physics of spin texture in nanoparticles involves competition between different energy terms in Eq. (3). In very small nanoparticles ($R << R_{coh}$), the exchange energy $A_e(\nabla \boldsymbol{S})^2 \sim A_e/R^2$ dominates and $\Theta(\boldsymbol{r})$ approaches zero as shown in Figs. 2(b) and 2(c), where R is the radius of the particle. The gradient term effectively suppresses magnetization inhomogeneities, scaling as $1/R^2$. However, as the particle size increases, nonuniform spin configurations emerge, exemplified by the top views in Figs. 2(e) and 2(f). This nonuniform state is referred to as the "flower state," in which the spins $\mathbf{S}(\mathbf{r})$ near the particle's edges form an angle $\Theta(\boldsymbol{r})$ with the symmetry axis [27,29,34]. As the radius further increases to a coherent radius R_{coh}, the flower state [29,31] competes against other spin states, such as curling states due to magnetostatic flux closure and decrease in energy density $A_e(\nabla \boldsymbol{S})^2$ which tends to keep spin parallel [27,29–31,33,34,49]. For $R > R_{coh}$ the nucleation is dominated by flux closure and realized by magnetization curling; in general flux closure is favorable as it decreases the energy of the system but competes against the exchange interaction. R_{coh} depends on magnetic material parameters and for the sphere and cylinder it is defined as $(R_{coh})_{sphere} = (5.09) \times l_{ex}$ and $(R_{coh})_{cylinder} = (3.36) \times l_{ex}$, respectively, where $l_{ex} = (A_e/\mu_0 M_s^2)^{1/2}$ is the exchange length [37,50]. It is unrelated to the single-domain size R_{SD}, which can be much larger than R_{coh} [34]. As shown in Figs. 1(e) and 1(f), the flower state and curling state can be viewed as the small part of Néel and Bloch skyrimions near the center, respectively, so their topological charge Q is less than $^1/_2$. In the subsequent sections, we will investigate Q and the topological Hall effect associated with the flower state and curling state, respectively.

A. Flower state

The flower state is predominantly observed in nonspherical particles, ideally cubes because the magnetization on these edges rotates away from the parallel orientation [31,37]. In our study, we investigated the function $\Theta(\boldsymbol{r})$ as a function of particle size and external magnetic field. The spin structure $\mathbf{S}(\mathbf{r})$ was determined by minimizing the micromagnetic (free) energy represented by Eq. (6):

$$\mathcal{E} = \int \eta \, \mathrm{d}V. \quad (7)$$

Here, the energy density η includes contributions from the exchange, anisotropy, Zeeman, and, for the flower-state contribution as described in Eq. (6). In general, the solution of the nonlinear differential equation can be done only numerically. The numerically calculated $\Theta(\boldsymbol{r})$ within the nanoparticle in Supplemental Material Fig. S2(a) shows that the spins exhibit a "radial" symmetry, tilting away from the z axis. The tilt angle increases with the distance from the center, illustrated by the spins at the particle edges or corners.

To gain insight into the physical aspects in a semiquantitative manner, we performed analytical calculations based on a set of simplifications to find the tilt angle $\Theta(R)$ at the edge in a magnetic nanoparticle of radius R. Firstly, we employed an approximate volume-averaging technique to simplify the energy integral as $\int \eta \mathrm{d}V = \langle\eta\rangle V$, where $\langle\eta\rangle$ represents the average energy density. Next, we minimized $\langle\eta\rangle$ with respect to $\Theta(R)$, which denotes the polar angle of the magnetization at the particle edges or corners; the length of the blue arrows in Fig. 2(d) is given by $\sin\Theta(R)$. Determining the precise value of the average $\langle\eta\rangle$ is highly challenging as it requires knowledge of $\mathbf{S}(\mathbf{r})$. However, $\mathbf{S}(\mathbf{r})$ is subject to certain constraints (normalization and symmetry) and is approximately known for several cases. By assuming small $\Theta(R)$, we find [see Supplemental Material Eqs. (S11)–(S13) [48]]

$$\langle\eta\rangle = \left[\frac{A_e}{R^2} + \left(K + \frac{\mu_0}{2}M_s H\right)\right][\sin^2\Theta(R)] - \frac{\mu_0}{2} M_s H_F \sin\Theta(R). \quad (8)$$

The interatomic exchange $\eta_A = A_e(\nabla \boldsymbol{S})^2$ scales as $A_e/R^2[\boldsymbol{S}_{xy}(\boldsymbol{r})^2] = A_e/R^2[\sin^2\Theta(R)]$; the second and third terms are anisotropy and Zeeman interaction contributions. The last term is the flower-state energy correction (H_F) due to nonuniform magnetization in Fig. 2(a). The flower state causes an xy component of the magnetostatic self-interaction. Essentially, the xy component of the stray field [green lines in Fig. 2(a)] contributes a Zeeman-type demagnetization energy, $\mu_0 H_F M_s |S_{xy}| \propto \mu_0 M_s H_F \sin\Theta(R)$. The parameter H_F depends on the shape of the particles, especially on the cross section, but is generally comparable to, though somewhat smaller than, the saturation magnetization M_s. While this field is zero for homogeneously magnetized ellipsoids, it is nonzero for magnetized particles of arbitrary shape (see Fig. 2). Overall, the flower state reduces the self-interaction energy compared with the homogeneous state. The self-interaction is $\boldsymbol{E}_d = -\mu_0 \boldsymbol{M}(\boldsymbol{r}) \cdot \boldsymbol{H}_d[\boldsymbol{M}(\boldsymbol{r})]/2$. For the homogeneous state, $\boldsymbol{E}_d = \mu_0 D\mathbf{M}^2/2$, whereas for the flower state, $\boldsymbol{E}_d < \mu_0 D\mathbf{M}^2/2$ due to tilted magnetization.

To identify the stable state, we minimize $\langle\eta\rangle$ using Eq. (8) with respect to $\Theta(R)$ for specific nanoparticles of radius R. As Eq. (8) is quadratic in $\sin\Theta(R)$, the minimization process

becomes straightforward. Explicitly, one has

$$\sin\Theta(R)=\frac{\mu_0 M_s H_F}{\frac{4A_e}{R^2}+4K+2\mu_0 M_s H}. \quad (9)$$

In Eq. (9), H_F is positive, meaning that the magnetization has a component pointing away from the symmetry axis. Equation (9) also shows that for small particles $\Theta(R)\to 0$ as $R\to 0$ and $\Theta(R)$ saturates when $R\to\infty$. Essentially, a larger $\Theta(R)$ requires smaller exchange energy, anisotropy energy, and Zeeman energy, but larger self-interaction energy. It is also clear that when the external field H is large enough, $\sin\Theta(R)$ diverges. $\Theta(R)$ for nanoparticles of different radius is plotted in Supplemental Material Fig. S2(b).

The Berry curvature can be determined through the application of Eq. (1) with respect to the $\mathbf{S}(\mathbf{r})$. Upon integrating the Berry curvature across the magnetic particle, the topological charge for the flower state can be found as

$$Q=\frac{1}{\pi}\Theta(R)=\frac{1}{\pi}\sin^{-1}\left(\frac{\mu_0 M_s H_F}{\frac{4A_e}{R^2}+4K+2\mu_0 M_s H}\right). \quad (10)$$

We conducted a comprehensive study on the topological charge, investigating its variation with particle radius at zero magnetic fields and with magnetic fields. Our findings are plotted in Figs. 3(a) and 3(b) for Q. Figure 3(a) exhibits a significant observation: for particles with radii much smaller than the characteristic coherence radius ($R << R_{coh}$), the topological charge remains nearly zero due to the dominant exchange term (A_e/R^2). However, as the particle size reaches a certain threshold, the topological charge undergoes a rapid increase and then gradually saturates near $R=R_{coh}$. At this point, the flower state ceases to exist, and instead, curling due to self-interaction becomes prominent. Although the specific transition size is influenced by micromagnetic parameters, we can qualitatively comprehend the overall trend using Eqs. (9) and (10).

In Fig. 3(b), we present the topological charge as a function of the magnetic field. Even in the high-field state, the system exhibits flower states akin to those depicted in Figs. 2(d)–2(f), but with a small Θ they closely resemble uniform magnetization as shown in Figs. 2(b) and 2(c). Notably, just before the magnetization reversal, the topological charge Q reaches its maximum value due to an increase in $\Theta(R)$. Furthermore, we calculated the emergent magnetic field due to the flower state in cylindrical nanoparticles at different positions in the xy plane, as shown in Fig. 4(a).

B. Magnetization curling

Magnetostatic interactions tend to favor a flux closure state ($\nabla\cdot\mathbf{M}\neq 0$) over magnetic poles ($\nabla\cdot\mathbf{M}=0$) [33,35]. During magnetization reversal, the "curling mode" emerges at the nucleation field when the particle radius exceeds R_{coh}. The curling state has finite helicity, and it represents the three-dimensional topological object [51]. Due to the flux closure property, the curling state does not require a correction to the self-interaction energy, as seen in the flower state (i.e., $H_F=0$). Instead, the demagnetization field $\boldsymbol{H}_d[\boldsymbol{M}(\boldsymbol{r})]$ provides the magnetostatic self-interaction necessary for flux closure. As

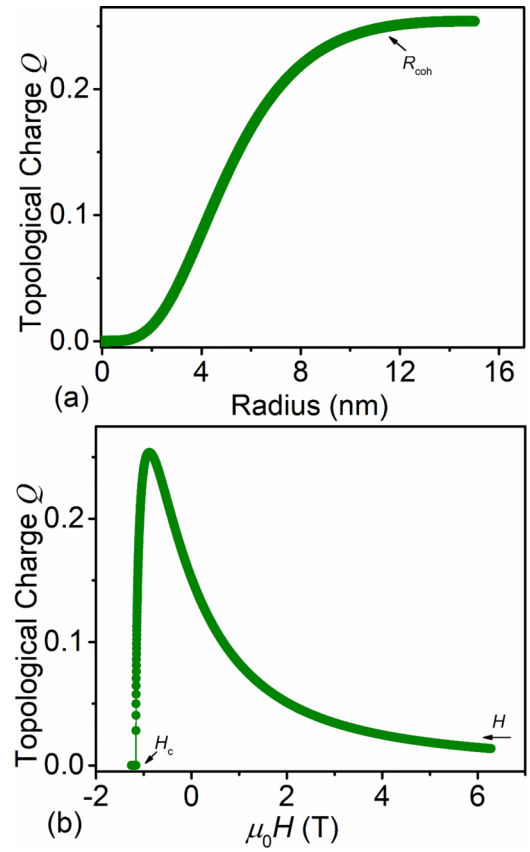

FIG. 3. Topological charge Q of magnetic nanoparticle particles with $R<R_{coh}$. (a) Particle-size dependence in the absence of an external magnetic field, where Q increases with particle size before it saturates at $R=R_{coh}$ when flower state is replaced by curling state. (b) Field dependence along half of the hysteresis loop, in which Q changes sign at the coercive field (H_c) with radius $R=10$ nm, i.e., $0.83R_{coh}$.

the size of nanoparticles increases, $|\boldsymbol{S}_{xy}(\boldsymbol{r})|$ increases, eventually leading to the transition into the curling state. $\boldsymbol{S}_{xy}(\boldsymbol{r})$ of the curling state can be obtained by minimizing the total energy, Eq. (6), with respect to $\boldsymbol{S}_{xy}(\boldsymbol{r})$ [29] [see Supplemental Material Eqs. (S14)–(S17) [48]]:

$$\left(2A_e\nabla^2-2K_1-\mu_0 M_s H+\mu_0 D M_s^2\right)\boldsymbol{S}_{xy}(\boldsymbol{r})=0. \quad (11)$$

In Eq. (11), $\boldsymbol{H}_d=-D\mathbf{M}$, where D represents the demagnetization factor contributing to flux closure. In the curling state, one has $\Phi(\boldsymbol{r})=\varphi\pm\pi/2$. Consequently, Eq. (4) can be rewritten as

$$\boldsymbol{M}(\boldsymbol{r})=M_s[-S_{xy}(\rho)\sin(\varphi)\boldsymbol{e}_x+S_{xy}(\rho)\cos(\varphi)\boldsymbol{e}_y+S_z\boldsymbol{e}_z], \quad (12)$$

where $S_{xy}(\rho)=\sin\Theta(\rho)$ and $S_z=\cos\Theta(\rho)$. Substituting the curling mode from Eq. (12) into Eq. (11) results in

$$\left(\rho^2\frac{\partial^2}{\partial\rho^2}+\rho\frac{\partial}{\partial\rho}+[(k\rho)^2-1]\right)S_{xy}(\rho)=0, \quad (13)$$

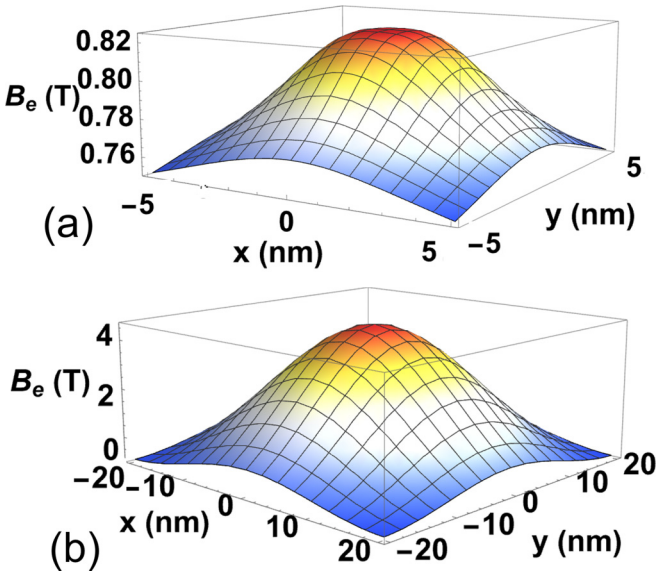

FIG. 4. Emergent magnetic field sensed by itinerant electrons in a nanoparticle at different positions in zero external magnetic field. (a) Particle of $R = 0.83R_{\rm coh}$ radius in a flower state. (b) Particle of $R = 1.6R_{\rm coh}$ radius in a curling state. Note the significant increase in field due to curling state as compared to flower state because of the topology associated with curling state helicity.

where k is defined as

$$k^2 = -\left(\frac{2K_1 + \mu_0 M_s H - \mu_0 M_s^2 D}{2A_e}\right). \tag{14}$$

Equation (13) is a Bessel equation, and as a result, the curling mode in a cylinder can be expressed as $S_{xy}(\rho) = J_1(k\rho)$ or approximately $\sin\Theta \approx \Theta(\rho) = J_1(k\rho)$. Figures 1(e) and S1 illustrate the curling mode vector three-dimensional plot within a cylinder, using $\sin\Theta \approx \Theta(\rho) = J_1(k\rho)$, $\Phi(\boldsymbol{r}) = \varphi \pm \pi/2$. Notice that we applied the boundary condition $\frac{\partial J_1(k\rho)}{\partial \rho}|_{\rho=R} = 0$, which leads to $kR = 1.841$ [29]. Moreover, when considering spherical particles with $D = 1/3$, the curling mode can be described using a spherical Bessel function $S_{xy}(\rho) = j_1(k\rho)$, where the smallest root is $kR = 2.0816$. The Berry curvature resulting from the curling in both the cylinder and the sphere are calculated using Eq. (1) as follows:

$$[B_c(\rho)]_{\rm cylinder} = \frac{J1(k\rho)}{\rho}\frac{\partial J_1(k\rho)}{\partial \rho}, \tag{15}$$

$$[B_c(r)]_{\rm sphere} = \frac{j_1(kr)}{r}\frac{\partial j_1(kr)}{\partial r}. \tag{16}$$

In Fig. 4(b), we present the emergent magnetic field Eq. (15) at the different points of the xy plane resulting from the curling mode of a cylinder. The Berry phase is obtained by integrating the Berry curvature:

$$\gamma_{\rm cylinder} = 2J_1(kR), \tag{17}$$

$$\gamma_{\rm sphere} = 2j_1(kR). \tag{18}$$

TABLE II. Calculated topological charge Q at the nucleation field.

	D	Smallest root (kR)	Bessel function	$Q(H_n)$
Cylinder	0	1.841	$J_1(1.841) = 0.58$	0.19
Sphere	1/3	2.0816	$j_1(2.081) = 0.44$	0.14

Similarly, we can calculate the topological charge for curling mode at the nucleation field by employing $\gamma = 2\pi Q$, as follows:

$$Q_{\rm cylinder} = \frac{1}{\pi}J_1(kR), \tag{19}$$

$$Q_{\rm sphere} = \frac{1}{\pi}j_1(kR). \tag{20}$$

At a field greater than the nucleation field, the particle with edges (like a cylinder) will exhibit a flower state with a small Θ, corresponding to a low topological charge. As the magnetic field decreases to the nucleation field, $H = H_n$, the transitions from the flower state to the curling state represent the field-dependent topological phase transition [51]. The helicity, topological charge, and consequently THE at the nucleation field undergo a significant increase. However, for particles with $R < R_{\rm coh}$, where only the flower state exists, there is no curling state at the nucleation field and as a result, no abrupt change in the topological charge occurs. These observations are also confirmed in micromagnetic simulations, as discussed in the next section. The nucleation field at which the curling appears is given by [44]

$$H_n = \frac{2K_1}{\mu_0 M_s} - DM_s + \frac{2A_e q_i^2}{\mu_0 M_s R^{2'}} \tag{21}$$

with q_i being the smallest root of Bessel functions. For cylinder $q_i = 1.841$ and for sphere $q_i = 2.0816$. By applying boundary conditions for cylinders and spheres and utilizing Bessel functions, we can calculate the topological charge Q for both shapes at the nucleation field. The resulting values are presented in Table II.

The topological charge listed above represents the exact value at the nucleation field for particles with $R = R_{\rm coh}$. To determine the corresponding THE at the nucleation field and for various particles at their respective nucleation fields, we can use Eq. (2). As a result, in nanoparticles at the nucleation field H_n, THE is expected to exhibit a sudden increase to $\rho_{\rm THE}(H_n)$ giving information related to nucleation field in nanoparticles.

For the $R > R_{\rm coh}$ where curling appears, Q has a constant value. It is because the curling mode is subject to the eigenvalue condition $kR = 1.84$ so $Q = 0.5J_1(1.84)^2 = 0.19$. This also applies to the following two considerations. The $J_1(kr)$ oscillations describe radial spin waves. The curling mode is a $1s$ state in the analogy of an electron in a cylinder, where the lowest-lying excited radial spin-wave mode is a $2s$ state and has $kR = 5.33$ and $Q = 0.06$ showing the Berry curvature of electron scattering from excited states is tricky from the viewpoint of dynamics [44].

As the R increases, $\boldsymbol{S}_{\rm xy}(\boldsymbol{r})$ also increases, eventually leading to a transition from the curling mode to the vortex mode. With the growth in size, the long-range magnetostatic

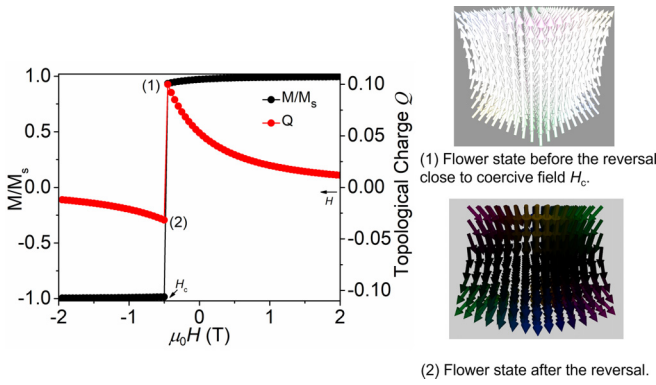

FIG. 5. Micromagnetic simulations of magnetization M and topological charge Q for a cubic ferromagnetic particle with a radius $R = 0.9R_{\text{coh}}$ less than R_{coh}. On the left is the field dependence of M and Q along half of the hysteresis loop, where Q reaches the maximum values near the coercive field H_c, which agrees with our theoretical prediction, Fig. 3(b), where finite H_F is responsible for a spin tilt at the edges. The deviation from the saturation appears just before the reversal shown in the inset. On the right are spin structures near H_c.

interaction between $\boldsymbol{M}(\boldsymbol{r})$ and $\boldsymbol{M}(\boldsymbol{r'})$ results in in-plane spin configurations. Consequently, the magnetostatic self-interaction becomes more important compared with the short-range exchange interactions.

C. Micromagnetic simulations and topological Hall effect

To investigate the topological spin textures in nanoparticles, we perform micromagnetic simulation, with a specific emphasis on regions close to R_{coh}. The simulations involve various shapes, including cubes, cylinders, and spheres. To explore the effect of size on the system, the radii of the cylinders and spheres were altered, and the topological charge and THE for different radii were simulated. During the process of magnetization reversal, we conducted calculations to determine the normalized magnetization and topological charge $Q(H)$. By applying Eq. (2) and the parameters in Table I, we utilized the obtained $Q(H)$ data to compute the Hall resistivity ρ_{THE} in cobalt (Co), iron (Fe), and nickel (Ni) spherical nanoparticles.

For the flower state, the topological charge was calculated for $R < R_{\text{coh}}$. The results demonstrated that the flower state only existed in either the cylinder or the ferromagnetic cube. In contrast, the sphere did not exhibit the flower state due to a small edge effect, where $H_F = 0$. Figure 5 depicts the hysteresis of the topological charge and normalized magnetization as a function of the decreasing/reverse field magnetic field $B(T) = \mu_0 H$ in a cube with a length less than the coherent radius. At higher magnetic fields, the spins aligned in the direction of the magnetic field, resulting in a lower value of the Q and hence Θ. Near the coercivity field, Q reached its maximum value just before the reversal, corresponding to the point of minimum magnetization and maximum opening of the flower state. The topological charge Q changed sign during the reversal, indicating a shift from $+\boldsymbol{M}_z$ to $-\boldsymbol{M}_z$ as the applied field changed from B_{max} to $-B_{\text{max}}$. Furthermore, the total Berry phase (γ) acquired by the electron is given by $\gamma = 2\pi Q$. The maximum value of Q at the coercive field is found to be 0.1 (toy model), and consequently, the value of $\gamma = 0.2\pi$. Therefore, we can deduce that the tilt angle at the coercive field in Fig. 5 is $\Theta = 0.5(\gamma) = 0.314$. From micromagnetic simulation, the tilt angle can be calculated as a function field $\Theta(H) = \pi Q(H)$.

Upon investigating nanoparticles with larger sizes $R > R_{\text{coh}}$, we observed a fascinating magnetization reversal phenomenon involving the curling mode. Utilizing micromagnetic simulations on our toy model of cylinders (Fig. 6) and spheres (Figs. 7–9) with radii greater than R_{coh}, we discovered the emergence of the curling mode during magnetization reversal at the nucleation field. In the case of cylinders with $R > R_{\text{coh}}$, we identified a field-dependent topological phase transition. Initially, the spin texture exhibited a flower state, where spins aligned with the direction of the strong external field, except for the tilted spins at the edges. However, the spin texture transitioned to a curling mode at nucleation field H_n with finite helicity, as indicated by the jump in magnetization and Q with core polarity aligned to the $+z$ axis. After magnetization reversal, the core polarity further realigned, now pointing in the direction of the $-z$ axis, accompanied by the curling mode of negative helicity. At high magnetic fields, the curling mode disappeared, and the system reverted to the flower state. It is worth noting that, unlike the cylinders, the spheres showed an absence of Q contributions at high magnetic fields, indicating the lack of a flower state in the spheres.

We have conducted a comprehensive study to investigate the topological Hall resistivity, Eq. (2), in spherical nanoparticles composed of Co, Fe, and Ni. This investigation was based on utilizing various parameters outlined in Table I and employing micromagnetic simulations, as displayed in Figs. 7 –9.

In the case of the spherical Co nanoparticle, intriguing phenomena were observed. Firstly, a curling state symmetric about the easy axis was observed at the nucleation field, as depicted in Fig. 7. As we decreased the reverse magnetic field, ρ_{THE} increased indicating an increase in planar magnetization. Additionally, we observe the emergence of an intermediate vortex state, wherein the magnetization of the core was oriented perpendicular to the easy axis as shown in Fig. 7. Following the intermediate state, the normal curling mode appeared with opposite helicity.

Figure 8 illustrates the ρ_{THE} of Fe, wherein intermediate states are absent. We observe the magnetization curling state at the nucleation field. As the reverse field is decreased, the magnitude of Q increases, indicating an increase in the in-plane component $\boldsymbol{S}_{\mathbf{xy}}(\boldsymbol{r})$. Once the reversal process begins, we observe the emergence of the curling mode with an opposite helicity. Finally, at high magnetic fields, the magnetic particles eventually reach saturation.

For spherical Ni nanoparticles, its negative anisotropy adds an intriguing dimension to magnetization reversal and the study of ρ_{THE}. Figure 9 illustrates that at the nucleation field, the curling mode emerges with a different helicity compared to that of Co and Fe. Additionally, ρ_{THE} exhibits an opposite sign, owing to the negative Hall coefficient. As the reverse field increases, ρ_{THE} also increases and causes a reversal

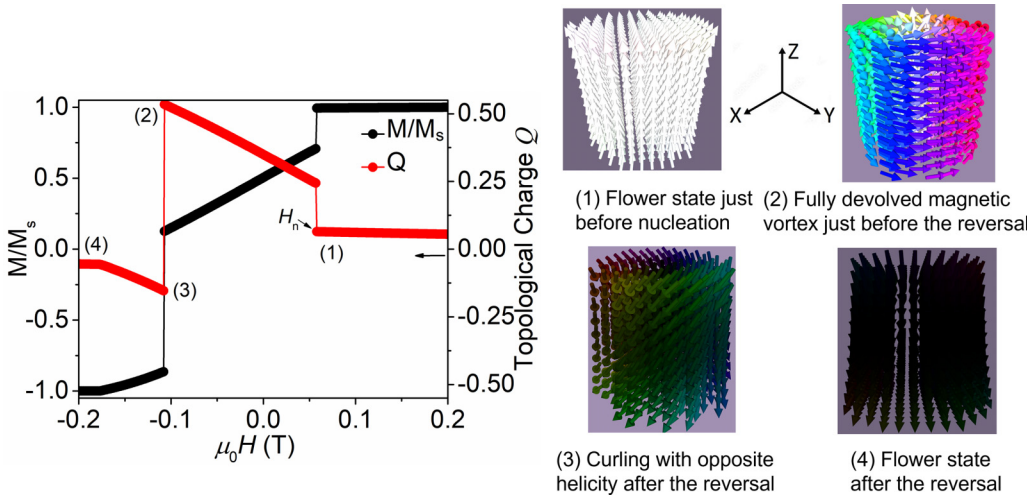

FIG. 6. Micromagnetic simulations of magnetization M and topological charge Q in a ferromagnetic cylinder with a radius $R = 1.2R_{\text{coh}}$ greater than R_{coh}. On the left is the field dependence of M and Q along half of the hysteresis loop, where a jump in topological charge at nucleation field H_{n} represents the transition from flower state to curling state. On the right are spin structures at different stages in the hysteresis loop.

in the sign of the topological Hall effect during magnetization reversal. Overall, these findings related to ρ_{THE} shed light on the complex behavior of nanoparticles with radius $R > R_{\text{coh}}$ during magnetization reversal, and highlight the importance of shape and size in determining their magnetic properties.

D. Magnetic force microscopy and topological Hall effect

According to our calculations, it is clear that the single-domain state leads to a finite emergent magnetic field and ρ_{THE}. Moreover, our micromagnetic simulation, as shown in Fig. 6, indicates that the flower state occurs at higher magnetic fields, while the curling state appears at lower fields,

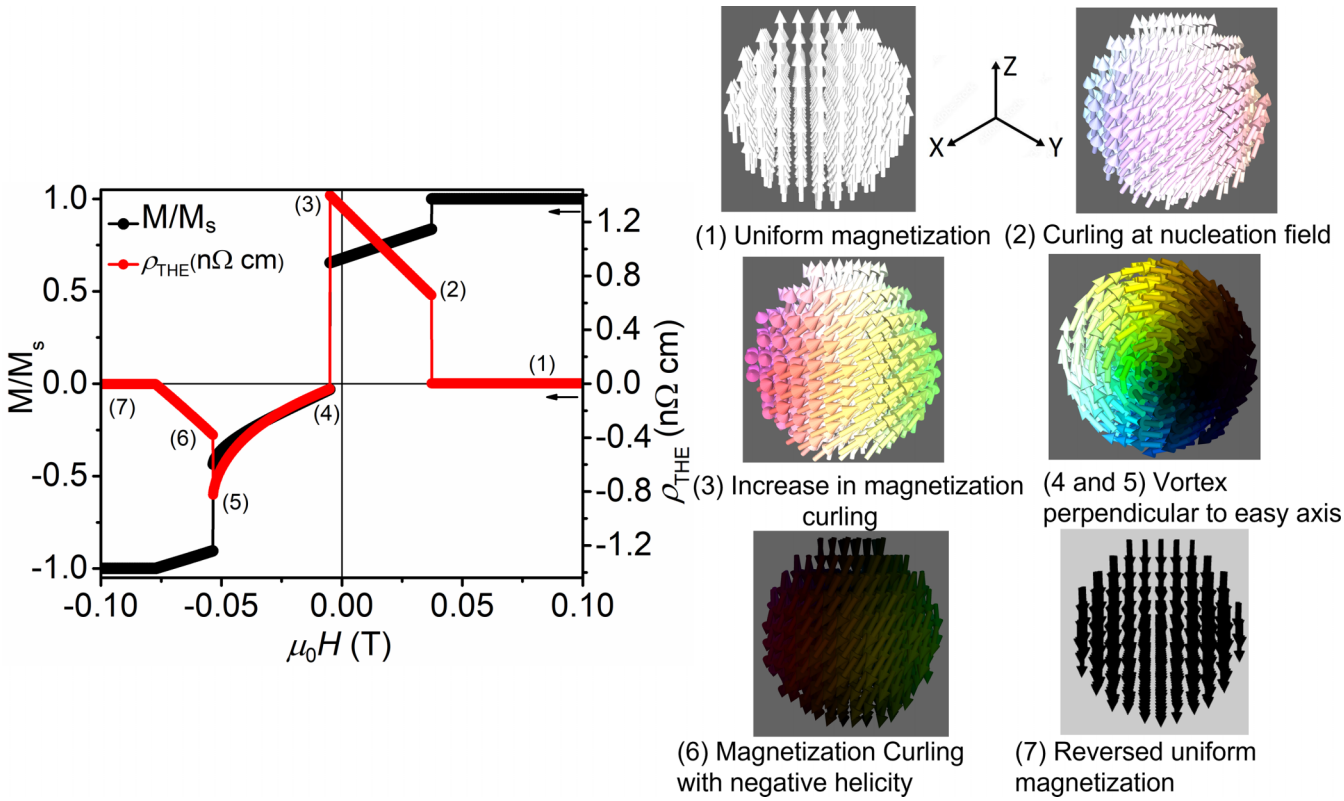

FIG. 7. Micromagnetic simulations of magnetization M and topological Hall resistivity ρ_{THE} in a spherical Co nanoparticle with radius $R = 14$ nm ($R > R_{\text{coh}}$). On the left is the field dependence of M and ρ_{THE} along half of the hysteresis loop. On the right is the spin structure at different stages in the hysteresis loop.

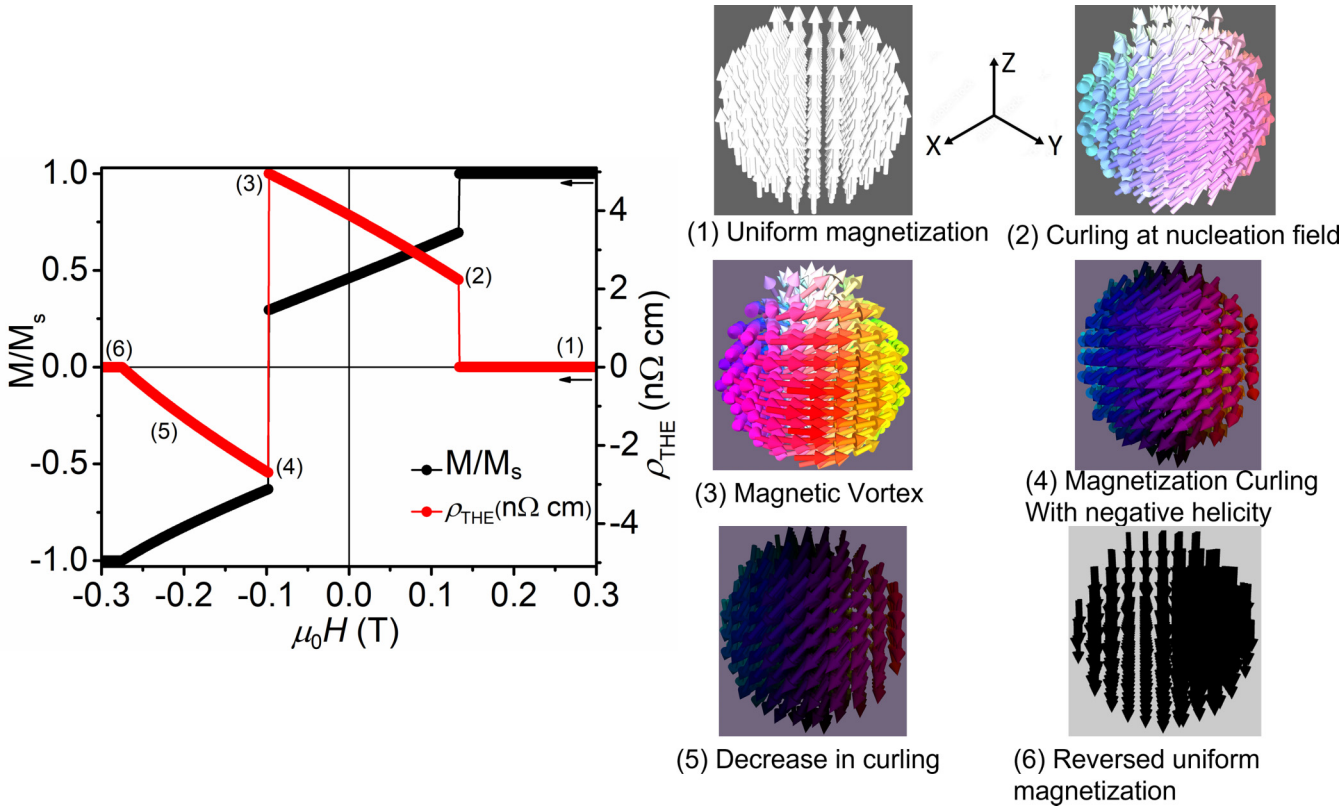

FIG. 8. Micromagnetic simulations of magnetization M and topological Hall resistivity ρ_{THE} in a spherical Fe nanoparticle with radius $R = 11$ nm ($R > R_{coh}$). On the left is the field dependence of M and ρ_{THE} along half of the hysteresis loop. On the right is the spin structure at different stages in the hysteresis loop.

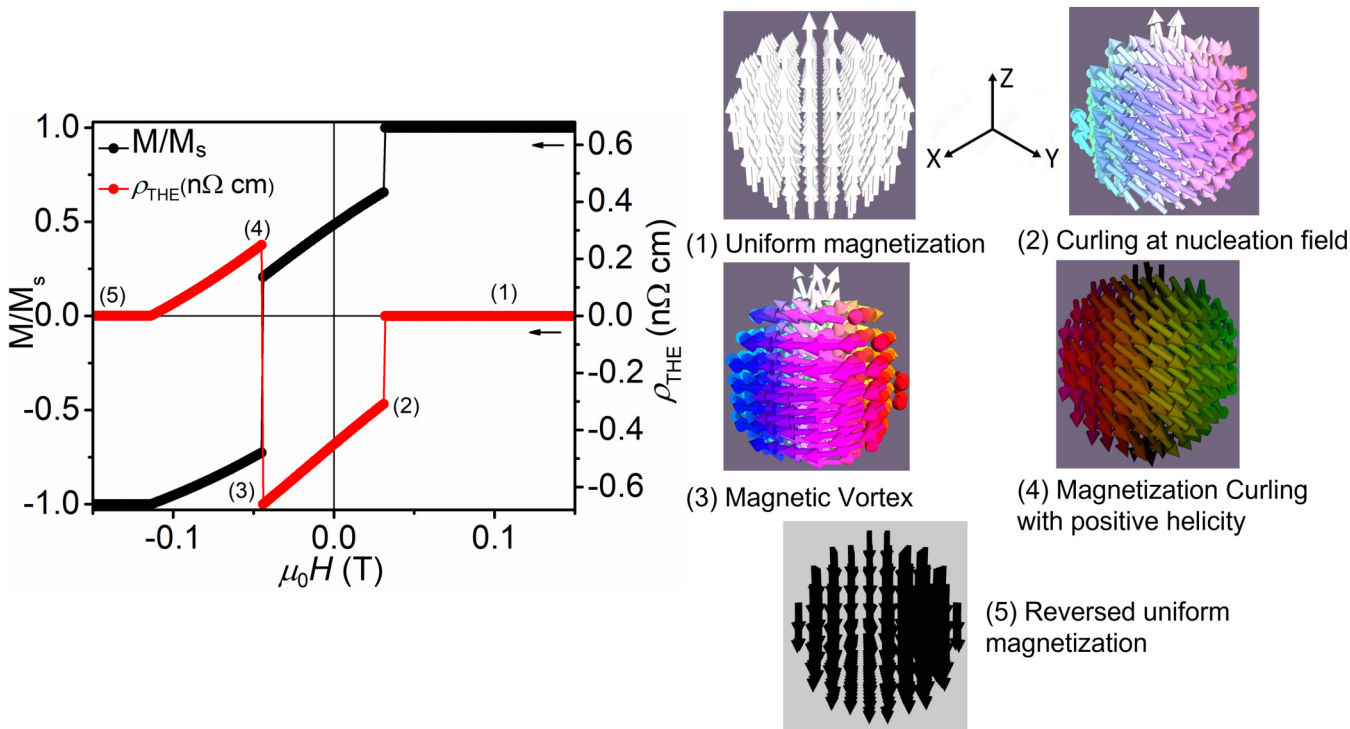

FIG. 9. Micromagnetic simulations of magnetization M and topological Hall resistivity ρ_{THE} in a spherical Ni nanoparticle with radius $R = 25$ nm ($R > R_{coh}$). On the left is the field dependence of M and ρ_{THE} along half of the hysteresis loop. On the right is the spin structure at different stages in the hysteresis loop.

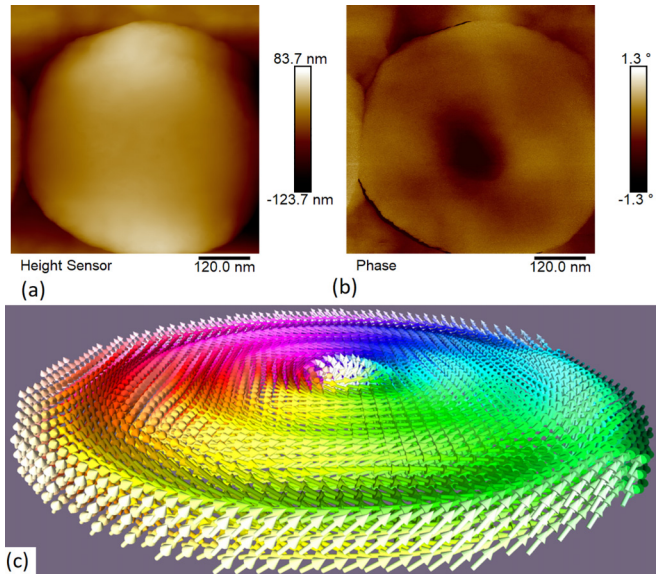

FIG. 10. (a) AFM image for a circular nanodot of Co. (b) MFM image of the nanodot in (a) showing the magnetic vortex core. (c) Micromagnetic simulation of the Co nanodisk of 480 nm diameter and 40 nm height showing the presence of vortex state.

provided that the particle's radius is in a single domain. To investigate the topological charge in confined geometries more thoroughly, we conducted MFM measurements on circular dots made of cobalt. These measurements provided strong evidence supporting the existence of a vortex state, which is characterized by a core magnetization perpendicular to the plane. The MFM and AFM images are displayed in Figs. 10 and 11. In most of the circular nanodots, the MFM images exhibit a clear contrast between the center and the surrounding regions. The spins within the dots are aligned parallel to the plane, but at the dark spot, the spin aligns perpendicular to the plane, as shown in Fig. 10(b). Our micromagnetic simulation, as depicted in Fig. 10(c), also supports the existence of a

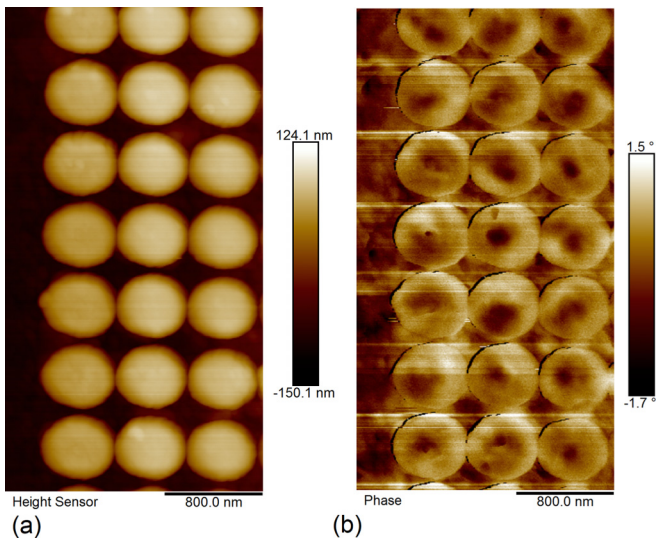

FIG. 11. (a) AFM image for an array of circular nanodots of Co. (b) MFM image of the nanodots in (a) showing the vortex states.

magnetic vortex state in cobalt nanodisks with a thickness of 40 nm and diameters up to 480 nm. This unique spin configuration in nanodots emerges when the dot thickness becomes smaller than the dot diameter, causing all spins to align in the plane, forming a vortex. It is worth noting that while the area of the dark region is relatively small for vortex states in materials like permalloy [49,52], the large anisotropy of cobalt results in a significantly larger dark spot area in the middle of the single-domain magnetic state. In Fig. 10(b), the MFM image and micromagnetic simulations show the presence of a finite topological charge Q within the nanodisk. As a result, we conducted calculations to determine the topological Hall resistivity, which yielded a low value of $\rho_{\mathrm{THE}} = 3 \times 10^{-3}\,\mathrm{n\Omega\,cm}$. It is noteworthy that this resistivity value is particularly small, especially when considering the relatively large area of the nanodisk.

Since in Fig. 11, the nanoparticles are very close to each other, this gives rise to a small exchange interaction between neighboring nanodisks and results in a tilted spin out of the plane at the edges. We performed a micromagnetic simulation of nanodisks close to each other. Our results are shown in Supplemental Material Fig. S5 and compared with Fig. 11(b).

In Supplemental Material Fig. S3, we observed that particles with a radius in the range of $R_{\mathrm{coh}} < R < R_{\mathrm{SD}}$, where R_{SD} is the radius of a single domain, exhibit two distinct states at different magnetic fields. At a high magnetic field, the presence of a finite topological charge is attributed to flower states, whereas at a low field, the configuration represents vortexlike spin textures. To further explore the effects of an external magnetic field, we applied a 0.9 T magnetic field perpendicular to the plane using permanent magnets. As shown in Supplemental Material Fig. S7, the vortexlike state vanishes, and most of the spins align in the direction of the field, except at the edges where the spins are slightly tilted, revealing the edge effects characteristic of the flower-state correction H_{F} for the spins at the edges.

IV. SUMMARY

We conducted a comprehensive investigation into the topological spin structures and the manifestation of electric transport in ferromagnetic nanoparticles, employing a combination of analytical calculations, micromagnetic simulations, and MFM imaging. Notably, in small nanoparticles with robust exchange stiffness, the typical flux closure state is absent and the flower state is present in particles with well-defined edges. To account for the flower state in nanoparticles, we introduced an energy correction term (H_{F}) into the micromagnetic free energy to consider the stray fields at the edges. This energy correction leads to a spin tilt at the edges and gives a finite topological charge (Q). We made a distinction between ellipsoidal (spherical) and nonellipsoidal (cubic and cylindrical) nanoparticles, with the latter exhibiting significant contributions to the topological charge from the flower state. We studied finite topological charge and THE, due to curling states both analytically and through micromagnetic simulations. The results unveiled a sudden jump in the Hall resistivity ρ_{THE}, attributed to the topological Hall effect, occurring at the nucleation field. The

manifestation of the topological Hall effect in Co, Fe, and Ni nanoparticles indicates a field-dependent topological phase transition from a uniform state to a curling state. These studies and results are in principle applicable to nanoparticles of all ferromagnetic material systems, suggesting potential applications. For instance, embedding individual magnetic particles in a nonmagnetic metallic matrix provides a potential experimental setup to explore these spin textures further in a wide range of ferromagnetic materials and for device applications in terms of their effect on electric transport.

ACKNOWLEDGMENTS

This research is primarily supported by the National Science Foundation under Grant No. OIA-2044049 (NSF-EQUATE). The research was performed in part in the Nebraska Nanoscale Facility: National Nanotechnology Coordinated Infrastructure and the Nebraska Center for Materials and Nanoscience (and/or NERCF), which are supported by the National Science Foundation under Award ECCS: 2025298, and the Nebraska Research Initiative. This work also used the Holland Computing Center of the University of Nebraska for performing micromagnetic simulations.

[1] Y. Tokura, M. Kawasaki, and N. Nagaosa, Nat. Phys. **13**, 1056 (2017).
[2] A. Fert, N. Reyren, and V. Cros, Nat. Rev. Mater. **2**, 17031 (2017).
[3] R. Wiesendanger, Nat. Rev. Mater. **1**, 16044 (2016).
[4] N. Nagaosa and Y. Tokura, Nat. Nanotechnol. **8**, 899 (2013).
[5] S. Seki and M. Mochizuki, *Skyrmions in Magnetic Materials* (Springer International, Cham, 2016).
[6] J. Bouaziz, H. Ishida, S. Lounis, and S. Blügel, Phys. Rev. Lett. **126**, 147203 (2021).
[7] A. Neubauer, C. Pfleiderer, B. Binz, A. Rosch, R. Ritz, P. G. Niklowitz, and P. Böni, Phys. Rev. Lett. **102**, 186602 (2009).
[8] B. Balasubramanian, P. Manchanda, R. Pahari, Z. Chen, W. Zhang, S. R. Valloppilly, X. Li, A. Sarella, L. Yue, A. Ullah, P. Dev, D. A. Muller, R. Skomski, G. C. Hadjipanayis, and D. J. Sellmyer, Phys. Rev. Lett. **124**, 057201 (2020).
[9] H. Zhang, D. Raftrey, Y.-T. Chan, Y.-T. Shao, R. Chen, X. Chen, X. Huang, J. T. Reichanadter, K. Dong, S. Susarla, L. Caretta, Z. Chen, J. Yao, P. Fischer, J. B. Neaton, W. Wu, D. A. Muller, R. J. Birgeneau, and R. Ramesh, Sci. Adv. **8**, eabm 7103 (2022).
[10] A. S. Ahmed, J. Rowland, B. D. Esser, S. R. Dunsiger, D. W. McComb, M. Randeria, and R. K. Kawakami, Phys. Rev. Mater. **2**, 041401(R) (2018).
[11] A. Soumyanarayanan, M. Raju, A. G. Oyarce, A. K. Tan, M.-Y. Im, A. Petrović, P. Ho, K. Khoo, M. Tran, and C. Gan, Nat. Mater. **16**, 898 (2017).
[12] A. A. Kovalev and S. Sandhoefner, Front. Phys. **6**, 98 (2018).
[13] Shi-Zeng Lin, A. Saxena, and C. D. Batista, Phys. Rev. B **91**, 224407 (2015).
[14] N. Gao, S.-G. Je, M.-Y. Im, J. W. Choi, M. Yang, Q. Li, T. Y. Wang, S. Lee, H.-S. Han, K.-S. Lee, W. Chao, C. Hwang, J. Li, and Z. Q. Qiu, Nat. Commun. **10**, 5603 (2019).
[15] J. Jena, B. Göbel, T. Hirosawa, S. A. Díaz, D. Wolf, T. Hinokihara, V. Kumar, I. Mertig, C. Felser, A. Lubk, D. Loss, and S. S. P. Parkin, Nat. Commun. **13**, 2348 (2022).
[16] N. Kanazawa, M. Kubota, A. Tsukazaki, Y. Kozuka, K. S. Takahashi, M. Kawasaki, M. Ichikawa, F. Kagawa, and Y. Tokura, Phys. Rev. B **91**, 041122(R) (2015).
[17] W. Zhang, B. Balasubramanian, A. Ullah, R. Pahari, X. Li, L. Yue, S. R. Valloppilly, A. Sokolov, R. Skomski, and D. J. Sellmyer, Appl. Phys. Lett. **115**, 172404 (2019).
[18] A. Ullah, X. Li, Y. Jin, R. Pahari, L. Yue, X. Xu, B. Balasubramanian, D. J. Sellmyer, and R. Skomski, Phys. Rev. B **106**, 134430 (2022).
[19] R. Pahari, B. Balasubramanian, A. Ullah, P. Manchanda, H. Komuro, R. Streubel, C. Klewe, S. R. Valloppilly, P. Shafer, P. Dev, R. Skomski, and D. J. Sellmyer, Phys. Rev. Mater. **5**, 124418 (2021).
[20] S. A. Majetich, T. Wen, and O. Thompson Mefford, MRS Bull. **38**, 899 (2013).
[21] https://phys.org/news/2022-03-magnetic-fields-3d-device-storage.html.
[22] K. Niitsu, Y. Liu, A. C. Booth, X. Yu, N. Mathur, M. J. Stolt, D. Shindo, S. Jin, J. Zang, N. Nagaosa, and Y. Tokura, Nat. Mater. **21**, 305 (2022).
[23] A. Ullah, B. Balamurugan, W. Zhang, D. J. Sellmyer, and R. Skomski, AIP Adv. **9**, 125049 (2019).
[24] I. E. Dzyaloshinskii, Sov. Phys. JETP **5**, 1259 (1957).
[25] T. Moriya, Phys. Rev. Lett. **4**, 228 (1960).
[26] T. Moriya, Phys. Rev. **120**, 91 (1960).
[27] W. F. Brown, Jr., *Micromagnetics* (Interscience Publishers, New York, 1963).
[28] E. H. Frei, S. Shtrikman, and D. Treves, Phys. Rev. **106**, 446 (1957).
[29] A. Aharoni, *Introduction to the Theory of Ferromagnetism* (Clarendon Press, Oxford, 1996).
[30] M. E. Schabes and H. N. Bertram, J. Appl. Phys. **64**, 1347 (1988).
[31] W. Rave, K. Fabian, and A. Hubert, J. Magn. Magn. Mater. **190**, 332 (1998).
[32] R. P. Cowburn and M. E. Welland, Appl. Phys. Lett. **72**, 2041 (1998).
[33] H. Kronmüller and M. Fähnle, *Micromagnetism and the Microstructure of Ferromagnetic Solids* (Cambridge University Press, Cambridge, 2003).
[34] R. Skomski, J. Phys.: Condens. Matter **15**, R841 (2003).
[35] R. Skomski, *Simple Models of Magnetism* (Oxford University Press, Oxford, 2008).
[36] J. M. D. Coey, *Magnetism and Magnetic Materials* (Cambridge University Press, New York, 2010).
[37] E. Pinilla-Cienfuegos, S. Mañas-Valero, A. Forment-Aliaga, and E. Coronado, ACS Nano **10**, 1764 (2016).
[38] K. Everschor-Sitte and M. Sitte, J. Appl. Phys. **115**, 172602 (2014).
[39] M. V. Berry, Proc. R. Soc. London, Ser. A **392**, 45 (1984).
[40] D. Xiao, M.-Ch. Chang, and Q. Niu, Berry phase effects on electronic properties, Rev. Mod. Phys. **82**, 1959 (2010).

[41] Y. Taguchi, Y. Oohara, H. Yoshizawa, N. Nagaosa, and Y. Tokura, Science **291**, 2573 (2001).
[42] A. Ullah, B. Balamurugan, W. Zhang, S. Valloppilly, X.-Z. Li, R. Pahari, L.-P. Yue, A. Sokolov, D. J. Sellmyer, and R. Skomski, IEEE Trans. Magn. **55**, 7100305 (2019).
[43] P. Bruno, V. K. Dugaev, and M. Taillefumier, Phys. Rev. Lett. **93**, 096806 (2004).
[44] R. Skomski, J. P. Liu, and D. J. Sellmyer, Phys. Rev. B **60**, 7359 (1999).
[45] M. Beg, M. Lang, and H. Fangohr, IEEE Trans. Magn. **58**, 7300205 (2022).
[46] M. J. Donahue and D. G. Porter, *OOMMF User's Guide, Version 1.0* (US Department of Commerce, National Institute of Standards and Technology, 1999).
[47] S. Lepadatu, J. Appl. Phys. **128**, 243902 (2020).
[48] See Supplemental Material at http://link.aps.org/supplemental/10.1103/PhysRevB.108.184432 for a comprehensive breakdown of the micromagnetic modeling calculations for both the flower state and curling state. Additionally, they include in-depth analyses of micromagnetic simulation results for a toy model and explanations of neighboring disk interactions on the magnetic vortex in a Co nanodisk. Furthermore, MFM images of the Co nanodisk illustrate the effects of external magnetic fields, showcasing micromagnetic simulations and confirming the presence of the flower state.
[49] T. Shinjo, T. Okuno, R. Hassdorf, K. Shigeto, and T. Ono, Science **289**, 930 (2000).
[50] R. Skomski, H.-P. Oepen, and J. Kirschner, Phys. Rev. B **58**, 3223 (1998).
[51] M. E. Schabes, J. Magn. Magn. Mater. **95**, 249 (1991).
[52] X. H. Zhang, T. R. Gao, L. Fang, S. Fackler, J. A. Borchers, B. J. Kirby, B. B. Maranville, S. E. Lofland, A. T. N'Diaye, E. Arenholz, A. Ullah, J. Cui, R. Skomski, and I. Takeuchi, J. Magn. Magn. Mater. **560**, 169627 (2022).